Revision 1

Discovery of the first natural hydride

Luca Bindi[1*], Fernando Cámara[2], William L. Griffin[3], Jin-Xiang Huang[3], Sarah E.M. Gain[3], Vered Toledo[4], Suzanne Y. O'Reilly[3]

[1]Dipartimento di Scienze della Terra, Università degli Studi di Firenze, Via G. La Pira 4, I-50121 Firenze, Italy
[2]Dipartimento di Scienze della Terra 'A. Desio', Università degli Studi di Milano, Via L. Mangiagalli 34, I-20133 Milano, Italy
[3]ARC Centre of Excellence for Core to Crust Fluid Systems (CCFS) and GEMOC, Earth and Planetary Sciences, Macquarie University, NSW 2109, Australia
[4]Shefa Yamim (A.T.M.) Ltd., Netanya 4210602, Israel

*Corresponding Author: luca.bindi@unifi.it

ABSTRACT

Although hydrogen is the most abundant element in the Solar System, the mechanisms of exchange of this element between the deep interior and surface of Earth are still uncertain. Hydrogen has profound effects on properties and processes on microscopic-to-global scales. Here we report the discovery of the first hydride (VH_2) ever reported in nature. This phase has been found in the ejecta of Cretaceous pyroclastic volcanoes on Mt Carmel, N. Israel, which include abundant xenoliths containing highly-reduced mineral assemblages. These xenoliths were sampled by their host magmas at different stages of their evolution but are not genetically related to them. The xenoliths are interpreted as the products of extended interaction between originally mafic magmas and CH_4+H_2 fluids, derived from a deeper, metal-saturated mantle. The last stages of melt evolution are recorded by coarse-grained aggregates of hibonite ($CaAl_{12}O_{19}$) + grossite ($CaAl_4O_7$) + V-rich spinels ± spheroidal to dendritic inclusions of metallic vanadium (V^0), apparently trapped as immiscible metallic melts. The presence of V^0 implies low oxygen fugacities, and suggests crystallization of the aggregates in a hydrogen-rich atmosphere. The presence of such reducing conditions in the upper

35   mantle has major implications for the transport of carbon, hydrogen and other volatile

36   species from the deep mantle to the surface.

INTRODUCTION

38   Evidence is rapidly accumulating for the widespread presence of highly-reduced

39   [low oxygen fugacity (fO$_2$)] volumes within the lithospheric mantle, both beneath

40   cratons and in off-craton areas with much thinner lithosphere (Griffin et al. 2018,

41   2019a). A key indicator of such low fO$_2$ is moissanite (SiC), which becomes stable at

42   fO$_2$ *ca* 6 log units below that of the Iron-Wustite buffer reaction (ΔIW -6). The IW

43   buffer is generally thought to define the minimum fO$_2$ of both the lithospheric mantle

44   and the deeper mantle (Frost and McCammon 2008). However, SiC with high-

45   temperature metallic inclusions is a relatively common trace phase in heavy-mineral

46   concentrates from kimberlites, lamproites and similar deep-seated volcanic rocks, and

47   occurs as an inclusion in diamonds (Shiryaev et al. 2011; Griffin et al. 2018, 2019a). It

48   has also been found in the peridotites and chromitites of many ophiolitic complexes,

49   particularly in the Tethyan belt across Tibet into Turkey, and in the Polar Urals. In these

50   complexes SiC is usually associated with a suite of other super-reduced (SuR) phases

51   including carbides, silicides and native metals (Fe, Cr, Ni) and in some cases,

52   microdiamonds with unusual morphology and isotopic characteristics (Xiong et al.

53   2017).

54   At least two off-craton occurrences, at Mt Carmel in northern Israel (Griffin et al.

55   2016, 2018; Xiong et al. 2017) and Sierra de Comechingones, Argentina (Cámara et al.

56   2019), now provide evidence for even lower fO$_2$, in the form of V^{2+}-bearing oxides, V-

57   Al alloys, and native vanadium in hibonite-grossite-spinel assemblages found as

58   xenolithic fragments in tuffs produced by explosive eruptions. The native metal requires

59   fO$_2$ of *ca* ΔIW -9, which suggests the presence of hydrogen-dominated fluids. Here we

60 confirm this suggestion by reporting the discovery of the first natural metal hydride,

61 VH_2, from the Mt Carmel locality, and discuss the implications for mantle fO_2 and the

62 transfer of fluids in the mantle.

SAMPLES

64   The xenoliths in which the natural hydride was found occur in the pyroclastic

65 ejecta of small Cretaceous basaltic volcanoes exposed on Mt Carmel, and have been

66 sampled from placer gemstone deposits in the Kishon river, which drains Mt Carmel

67 and enters the sea near Haifa in northern Israel (Griffin et al. 2018). They are part of a

68 xenolith assemblage that includes aggregates of skeletal corundum crystals with melt

69 pockets containing reduced mineral assemblages [SiC (moissanite), Fe-Ti-Zr

70 silicides/phosphides, Ti-nitrides and borides] that require high T and very low fO_2

71 (down to $\leq \Delta IW$ -7). The xenoliths studied here comprise coarse-grained aggregates of

72 hibonite+grossite+spinel assemblages that carry inclusions of V^0 and V-Al alloys,

73 indicating fO_2 down to $\leq \Delta IW$ -9. Descriptions of these rocks (Griffin et al. 2016, 2018,

74 2019a, 2019b; Xiong et al. 2017) have noted the abundance of amorphous carbon in

75 brecciated aggregates, and SiC and TiC in the xenoliths, and suggested that the

76 crystallization of skeletal corundum and the unusually low fO_2 reflect the interaction of

77 deep-seated basaltic magmas with mantle-derived CH_4+H_2 at high fluid/melt ratios.

78 This interaction led to progressive reduction, desilication of the magma through the

79 immiscible separation of carbon-rich Fe-Ti-silicide melts (abundant in the corundum

80 aggregates), and ultimately to Al_2O_3-supersaturation and the rapid growth of

81 skeletal/hopper corundum crystals, which have trapped samples of their parental melts.

82   The coarse (cm-size crystals) V-bearing hibonite+grossite+spinel aggregates

83 discussed here appear to represent a late, pegmatitic stage of this evolution (Griffin et

84 al. 2019b). The grain sizes, magmatic microstructures, and evidence for an extended

3

85   sequence of magmatic crystallization (Xiong et al. 2017; Griffin et al. 2018) clearly rule

86   out more speculative origins such as lightning strikes (Ballhaus et al. 2017), meteorite

87   impact, or shallow hydrothermal circulation. Petrographic evidence for the reaction

88   liquid + corundum → anorthite, and the stability of grossite, suggest that this process

89   operated at or near to the base of the crust (25-30 km depth; Griffin et al. 2018), and at

90   temperatures ranging from 1450-1500 °C to a minimum of >1150 °C (see below).

91

RESULTS AND DISCUSSION

Occurrence of vanadium hydride (VH_2)

94   The new vanadium hydride was found as one subhedral crystal, about 20 μm in

95   size, coexisting with V^0 and (V-Al)-alloys enclosed in hibonite (Figure 1). Microprobe

96   analysis of this grain (carried out using a CAMECA 100X electron microprobe at 15

97   kV, 10 nA, 1 μm beam size, counting times 20 s for peak and 10 s for background)

98   showed only V, with minor Al (~5 at.%).

99   To get information on the crystal structure, the small VH_2 fragment was

100   handpicked from the polished section under a reflected light microscope and mounted

101   on a 5 μm diameter carbon fiber, which was, in turn, attached to a glass rod. Then, the

102   fragment was tested by single-crystal X-ray diffraction. Single-crystal X-ray studies

103   were carried out using a Bruker D8 Venture diffractometer equipped with a Photon III

104   CCD detector, with graphite-monochromatized Mo$K\alpha$ radiation (λ = 0.71073 Å), and

105   with 100 s exposure time per frame; the detector-to-sample distance was 7 cm.

106   Since we have only one grain, we have avoided destructive analysis to quantify

107   the hydrogen content. The structural data (see below) represent a strong and solid proof

108   in support of the VH_2 stoichiometry.

109

Crystal structure of VH$_2$

110

111   The structure was solved by direct methods and then refined using the program

112   Shelxl-97 (Sheldrick 2008). The site occupation factor (s.o.f.) at the V site was allowed

113   to vary (V vs. Al) using scattering curves for neutral atoms taken from the International

114   Tables for Crystallography (Wilson 1992). At the last refinement stage, with anisotropic

115   atomic displacement parameters for V and no constraints, the residual value settled at

116      $R_1(F) = 0.0134$ for 25 unique reflections and 4 parameters.

117   Crystallographic data (CCDC 1870868) can be obtained free of charge from *The*

118   *Cambridge Crystallographic Data Centre* via www.ccdc.cam.ac.uk/data_request/cif

119   and are available as supplementary material[1].

120   The crystal structure of VH$_2$ is shown in Figure 2. It shows a cubic unit-cell [$a =$

121   4.268(1) Å; $Z = 4$] and space group *Fm-3m*, with the CaF$_2$ structure type. The solution

122   of the crystal structure gave the VH$_2$ stoichiometry, with minor Al substituting for V

123   (i.e., V$_{0.96}$Al$_{0.04}$), in excellent agreement with the electron microprobe data. The results

124   obtained are in excellent agreement with what has been reported for synthetic VH$_2$

125   (Müller and Weymann 1986).

126

Thermodynamics of vanadium hydrides

127

128   According to Yukawa et al. (2002), vanadium metal absorbs hydrogen and forms

129   first the β_1 phase (V$_2$H low-temperature phase). Then, as the hydrogenation proceeds,

130   the first order phase transition from the β_1 phase to the β_2 phase (V$_2$H high-temperature

131   phase) or γ' (VH) takes place. Finally, the γ phase (VH$_2$) is formed when it is fully

132   hydrogenated. As a result, there exist two plateaus in the PCT (pressure-composition-

133   temperature) curve of the V-H system. The first plateau corresponds to the coexistence

---

[1] For a copy of CIF, document item ……., contact the Business Office of the Mineralogical Society of America.

5

134   of the α phase (hydrogen solid solution phase) and the β_1 phase. However, the β_1 phase

135   is so stable that the first plateau pressure for this hydride formation is as low as 0.1 Pa at

136   moderate temperatures. Therefore, the hydrogen desorption reaction from the β_1 phase

137   never occurs under moderate conditions, for example, at room temperature. On the other

138   hand, the second plateau marks to the coexistence of the β_2 phase (VH) and the γ phase,

139   VH_2, which corresponds to the natural compound we have identified. As the γ phase is

140   not so stable, its hydrogen absorption and desorption reactions can take place at

141   moderate temperatures and pressures. For this reason, only about half of the hydrogen

142   dissolved in vanadium metal can be used in the subsequent hydrogen absorption and

143   desorption processes.

144

145   **Vanadium hydrides at high pressure and temperature**

146   Vanadium hydrides are usually prepared electrolytically by heating vanadium

147   metal with hydrogen (Müller and Weymann 1986). Therefore, the observed abundance

148   of V^0 and V-Al alloys in our samples may suggest that VH_2 formed by a localized

149   reaction in the presence of free hydrogen. Suzuki et al. (1989) studied the system

150   (transition metal)-silicate-water at pressures of around 5 GPa and at temperatures

151   ranging from 1000 to 1300 °C using a tetrahedral-anvil high-pressure apparatus and

152   quenching the products isobarically. In their study of the system V-silicate-water they

153   observed the formation of V-oxide dendrites enclosed in vanadium dihydride, VH_2. The

154   petrographic relationships between the two phases clearly showed that hydrogen and

155   oxygen coexisted, dissolved in liquid vanadium, at high pressure and temperature. Such

156   a scenario might be applicable to what is observed in the Mt Carmel samples but with

157   some differences. We found metallic vanadium and (V-Al)-alloys instead of V-oxides,

158   indicating an almost anoxic environment. However, some of the metal inclusions show

159 typical "dense branching structures" (dendrites) (Müller and Weymann 1986; Griffin et

160 al. 2019a) and are associated with sporadic VH_2. This represents striking evidence that

161 free hydrogen was present and that it was able to form some VH_2 from V^0.

162   Experimental data on the V-H system at magmatic temperatures are extremely

163 sparse, but Fukai (2005) has published a phase diagram for 5 GPa. The melting point of

164 pure vanadium is >1900 °C at 1 atm, rising to *ca* 2100 °C at 5 GPa (Figure 3).

165 However, H is highly soluble in vanadium melts, and lowers the melting point

166 dramatically; the α phase coexisting with the γ' phase (VH) at the eutectic at *ca* 1050 °C

167 has the composition $V_{0.7}H_{0.3}$. In more H-rich compositions VH is on the liquidus down

168 to a peritectic at *ca* 775 °C, where it reacts with the melt to form the γ phase VH_2; this

169 remains the liquidus phase down to *ca* 250 °C, and is stable as a solid phase to very low

170 *T*. At 1 GPa (the approximate pressure of the Mt Carmel magmatic system; Griffin et al.

171 2018) these would represent maximum temperatures, assuming that the general pattern

172 of phase relationships shown in Figure 3 remains the same.

173   The minimum temperature of the Mt Carmel hibonite-grossite-spinel-vanadium

174 assemblages before entrainment and eruption in the host basaltic magmas is constrained

175 by the coexistence of hibonite+grossite + fluorite of the phase $Ca_2Al_3O_6F_2$, which is not

176 stable below 1150 °C at 1 atm (Kim 2011). It therefore is unlikely that the VH_2 sampled

177 here was a liquidus phase. However, as the higher-*T* vanadium melts cool and

178 crystallize following eruption, they will lose their dissolved H_2 (Fukai 2005); no H has

179 been observed in three large V balls analyzed by single-crystal X-ray diffraction

180 (Griffin et al. 2019b). We suggest that some of this expelled H_2 may have been trapped

181 in the outer portions of the melt inclusions, and especially in the sort of smaller

182 protuberances seen in Figure 1. With increasing H/V ratios, this would lead to the

183 subsolidus formation first of VH, then of VH_2, and eventually to the remelting and

7
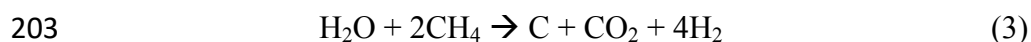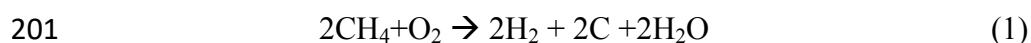
184   redistribution of VH_2, as suggested by the apparent intrusion of "vanadium" melt into

185   the surrounding grossite and fluorite (Figure 1).

186

187   **Generation of free hydrogen in the mantle**

188   The fluids involved in the generation of the ultra-reduced assemblages described

189   here presumably are derived from greater depths, and transported upward in association

190   with mantle-derived magmas. The magmas that carried Mt Carmel samples to the

191   surface have been ascribed to "hot-spot" volcanism and carry OIB trace-element and

192   isotopic signatures (Stein and Hofmann 1992). If the sub-lithospheric mantle source of

193   such magmas is metal-saturated (e.g. $\Delta IW = 0$), then any C-O-H fluid will be dominated

194   by CH_4, with significant contents of H_2 and lesser amounts of H_2O (Frost and

195   McCammon 2008; Matveev et al. 1997). If such fluids are removed to shallower levels,

196   they will either be oxidized by the surrounding FeO-bearing mantle, or will impose a

197   low fO_2 on their wall rocks, depending the local fluid/rock ratio. The oxidation of CH_4

198   to produce "syngas" is a well-understood industrial process; at pressures >3 kb, where

199   generation of CO is suppressed, it can proceed by reactions such as:

200

201                 $2CH_4 + O_2 \rightarrow 2H_2 + 2C + 2H_2O$ (1)

202   SiO_2 (in silicates) $+ CH_4 \rightarrow SiC + 2H_2O$ (2)

203                 $H_2O + 2CH_4 \rightarrow C + CO_2 + 4H_2$ (3)

204

205   These reactions are consistent with the abundance of SiC and amorphous carbon in in

206   the Mt Carmel assemblages (Griffin et al. 2018). At mantle depths, H_2 and H_2O are

207   immiscible (Bali et al. 2014); the liberated H_2 would be available to drive further

8

208 reduction of the local environment to at least ΔIW -9, and to have a major impact on

209 phase relations in coexisting melts and solids.

210   An alternative mechanism for generating CH_4-rich fluids (Golubkova et al. 2016)

211 is based on the extraction of oxygen from graphite-saturated COH fluids by oxidation of

212 Fe^{2+}, or by removal of carbonate or hydrous phases. Significantly, neither the Mt

213 Carmel nor the Argentinian V-bearing assemblages contain any hydrous phases or

214 carbonates, and none of the oxide or silicate phases in the Mt Carmel corundum

215 xenoliths contain Fe, as all Fe is sequestered in immiscible Fe-Ti-Si-C melts (Griffin et

216 al. 2018). However, mechanisms like that proposed by Golubkova et al. (2016) may

217 have been operative in the early stages of the evolution of the fluid-melt system and this

218 needs further investigation.

219

220   **IMPLICATIONS**

221 The evidence for the presence of CH_4+H_2-dominated fluids at Mt Carmel (and

222 elsewhere; Griffin et al. 2018) is a strong argument for the presence of a free metal

223 phase in the sub-lithospheric mantle, buffering fO_2 near IW. This is consistent with

224 other lines of evidence, both theoretical (Rohrbach et al. 2007; Frost and McCammon

225 2008; Stagno et al. 2013) and physical, in the form of metallic inclusions (accompanied

226 by CH_4+H_2) in sub-lithospheric Type II diamonds (Smith et al. 2016, 2018). The

227 movement of such fluids to shallower depths, perhaps through deep-seated volcanism,

228 would allow them to interact with the subcontinental lithosphere, and play an important

229 role in the deposition of carbon as amorphous carbon, graphite or diamonds, depending

230 on the depth of oxidation. The oxidation products of these reactions (CO_2 and H_2O)

231 may ultimately play an important role in mantle metasomatism (Griffin et al. 2018,

232 2019a). The presence and movements of such reducing fluids in the upper mantle have

9

233   major implications for the transport of carbon, hydrogen and other volatile species from

234   the deep mantle to the surface.

235

244

245   **REFERENCES CITED**

246   Bali, E., Audetat, A., and Keppler, H. (2014) Water and hydrogen are immiscible in

247   Earth's mantle. Nature, 495, 220–223.

248   Ballhaus, C., Wirth, R., Fonseca, R.O.C., Blanchard, H., Pröll, W., Bragagni, A., Nagel,

249   T., Schreiber, A., Dittrich, S., Thome, V., Hezel, D.C., Below, R., and Cieszynski,

250   H. (2017) Ultra-high pressure and ultra-reduced minerals in ophiolites may form

251   by lightning strikes. Geochemical Perspective Letters, 5, 42–46.

252   Cámara, F., Bindi, L., Pagano, R., Pagano, A., Gain, S.E.M., and Griffin, W.L. (2019)

253   Dellagiustaite: A novel natural spinel containing V^{2+}. Minerals, 9, 4–20.

254   Frost, D.J., and McCammon, C.A. (2008) The redox state of Earth's mantle. Annual

255   Review of Earth and Planetary Sciences, 36, 389–420.

256   Fukai, Y. (2005) The Metal-Hydrogen System: Basic Bulk Properties. Springer-Verlag,

257   Berlin, 500 pp.

258   Golubkova, A., Schmidt, M.W., and Connolly, J.A.D. (2016) Ultra-reducing conditions

259   in average mantle peridotites and in podiform chromitites: a thermodynaic model

260   for moissanite (SiC) formation. Contributions to Mineralogy and Petrology 171,

261   41–58.

262   Griffin, W.L., Gain, S.E.M., Adams, D.T., Huang, J.-X., Saunders, M., Toledo, V.,

263   Pearson, N.J., and O'Reilly, S.Y. (2016) First terrestrial occurrence of tistarite

264   (Ti_2O_3): Ultra-low oxygen fugacity in the upper mantle beneath Mt. Carmel,

265   Israel. Geology, 44, 815–818.

266   Griffin, W.L., Huang, J.-X., Thomassot, E., Gain, S.E.M., Toledo, V., and O'Reilly,

267   S.Y. (2018) Super-reducing conditions in ancient and modern volcanic systems:

268   Sources and behaviour of carbon-rich fluids in the lithospheric mantle.

269   Mineralogy and Petrology, 112, 1–14.

270   Griffin, W.L., Gain, S.E.M., Huang, J.-X., Saunders, M., Shaw, J., Toledo, V., and

271   O'Reilly, S.Y. (2019a) A terrestrial magmatic hibonite-grossite-vanadium

272   assemblage: Desilication and extreme reduction in a volcanic plumbing system,

273   Mt Carmel, Israel. American Mineralogist, 103, doi:10.2138/am-2019-6733.

274   Griffin, W. L., Gain, S.E.M., Bindi, L., Shaw, J., Saunders, M., Huang, J-X., Camara,

275   F., Toledo, V., and O'Reilly, S.Y. (2019b) Extreme reduction: Vanadium melts in

276   mantle-derived oxide xenoliths. Geochemical Perspective Letters (in review).

277   Kim, D-G. (2011) Experimental Study and Thermodynamic Modelling of the CaO-

278   SiO_2-Al_2O_3-CaF_2 System. Master Thesis, McGill University Libraries.

279   Matveev, S., Ballhaus, C., Fricke, K., Truckenbrodt, J., and Ziegenben, D. (1997)

280   Volatiles in the Earth's mantle. 1. Synthesis of CHO fluids at 1273 K and 2.4

281   GPa. Geochimica et Cosmochimica Acta, 61, 3081–3088.

282   Müller, H., and Weymann, K. (1986) Investigation of the ternary systems Nb-V-H and

283   Ta-V-H. Journal of Less Common Metals, 119, 115–126.

284   Rohrbach, A., Ballhaus, C., Golla-Schindler, U., Ulmer, P., Kamenetsky, V.S., and

285   Kuzmin D.V. (2007) Metal saturation in the upper mantle. Nature, 449, 456–458.

286   Sheldrick, G.M. (2008) A short history of SHELX. Acta Crystallographica, A64, 112–

287   122.

288   Shiryaev, A.A., Griffin, W.L., and Stoyanov, E. (2011) Moissanite (SiC) from

289   kimberlites: polytypes, trace elements, inclusions and speculations on origin.

290   Lithos, 122, 152–164.

291   Smith, E.M., Shirey, S.B., Nestola, F., Bullock, E.S., Wang, J., Richardson, S.H., and

292   Wang, W. (2016) Large gem diamonds from metallic liquid in Earth's deep

293   mantle. Science, 354, 1403–1405.

294   Smith E.M., Shirey, S.B., Richardson, S.H., Nestola, F., Bullock, E.S., Wang, J., and

295   Wang, W. (2018) Blue boron-bearing diamonds from Earth's lower mantle.

296   Nature, 560, 84–87.

297   Stagno, V., Ojwang, D.O., McCammon, C.A., and Frost, D.J. (2013) The oxidation

298   state of the mantle and the extraction of carbon from Earth's interior. Nature, 493,

299   84–88.

300   Stein, M., and Hofmann, A.W. (1992) Fossil plume head beneath the Arabian

301   lithosphere? Earth and Planetary Science Letters, 114, 193–209.

302   Suzuki, T., Akimoto, S.-I., and Yagi, T. (1989) Metal-silicate-water reaction under high

303   pressure. I. Formation of metal hydride and implications for composition of the

304   core and mantle. Physics of the Earth and Planetary Interiors, 56, 377–388.

305   Wilson, A.J.C. Ed. (1992) International Tables for Crystallography, Volume C:

306   Mathematical, physical and chemical tables. Kluwer Academic, Dordrecht, NL.

307 Xiong, Q., Griffin, W.L., Huang, J.-X., Gain, S.E.M., Toledo, V., Pearson, N.J., and

308   O'Reilly, S.Y. (2017) Super-reduced mineral assemblages in "ophiolitic"

309   chromitites and peridotites: the view from Mt. Carmel. European Journal of

310   Mineralogy, 29, 557–570.

311 Yukawa, H., Takagi, M., Teshima, A., and Morinaga, M. (2002) Alloying effects on the

312   stability of vanadium hydrides. Journal of Alloys and Compounds, 330-332, 105–

313   109.

314

315

316

317

318

319

320

321

322

323

324

325

326

327

328

329

330

331

332   **FIGURE CAPTIONS**

333   **Figure 1.** Images of the rock fragment from Mt Carmel. (a) Back-scattered electron

334   image of the hibonite-grossite-spinel aggregate studied. The red box

335   indicates the region enlarged in (b) and (c), which represent X-ray

336   compositional maps. (d) Transmitted-light photo (plane polars) of the rock

337   sample studied, showing inclusions of metallic vanadium in platy hibonite

338   crystals. The white dashed box indicates the region enlarged in (e), which is

339   also shown as back-scattered electron image (f). Arrows mark the (V,Al)-

340   alloys and the VH_2 fragment that was sampled.

341   **Figure 2.** The crystal structure of VH_2. Dark green and light grey spheres correspond to

342   V and H atoms, respectively. The unit cell and the orientation of the

343   structure are outlined.

344   **Figure 3.** Phase diagram of the V-H system at *ca* 5 GPa. Diagram redrawn after Fukai

345   (2005). The minimum crystallization temperature (red dashed line) of the

346   oxide-fluoride phases of the matrix is constrained by the presence of

347          $Ca_2Al_3O_6F_2$.

348

349

a) **1 mm**

b) Al F

c) Ca₄Al₆O₁₂F₂ Ca V

V

Fl

Gros

Hbn

d)

e)

f) VH₂ (V,Al)-alloy

100 μm